



# Models of gravitational lens candidates from Space Warps CFHTLS

Rafael Küng,<sup>1</sup>★ Prasenjit Saha,<sup>1</sup>★ Ignacio Ferreras,<sup>2</sup> Elisabeth Baeten,<sup>3</sup>  
 Jonathan Coles,<sup>4</sup> Claude Cornen,<sup>3</sup> Christine Macmillan,<sup>3</sup> Phil Marshall,<sup>5</sup>  
 Anupreeta More,<sup>6</sup> Lucy Oswald,<sup>7</sup> Aprajita Verma<sup>8</sup> and Julianne K. Wilcox<sup>3</sup>

<sup>1</sup>Physik-Institut, University of Zurich, Winterthurerstrasse 190, CH-8057 Zurich, Switzerland

<sup>2</sup>Mullard Space Science Laboratory, University College London, Holmbury St Mary, Dorking, Surrey RH5 6NT, UK

<sup>3</sup>Zooniverse, c/o Astrophysics Department, University of Oxford, Oxford OX1 3RH, UK

<sup>4</sup>Physik-Department, Technische Universität München James-Franck-Str. 1, D-85748 Garching, Germany

<sup>5</sup>Kavli Institute for Particle Astrophysics and Cosmology, Stanford University, 452 Lomita Mall, Stanford, CA 94035, USA

<sup>6</sup>Kavli IPMU (WPI), UTIAS, University of Tokyo, Kashiwa, Chiba 277-8583, Japan

<sup>7</sup>Murray Edwards College, University of Cambridge, Cambridge CB3 0DF, UK

<sup>8</sup>Sub-department of Astrophysics, University of Oxford, Denys Wilkinson Building, Keble Road, Oxford, OX1 3RH, UK

Accepted 2017 November 19. Received 2017 November 19; in original form 2017 May 2

## ABSTRACT

We report modelling follow-up of recently discovered gravitational-lens candidates in the Canada France Hawaii Telescope Legacy Survey. Lens modelling was done by a small group of specially interested volunteers from the Space Warps citizen-science community who originally found the candidate lenses. Models are categorized according to seven diagnostics indicating (a) the image morphology and how clear or indistinct it is, (b) whether the mass map and synthetic lensed image appear to be plausible, and (c) how the lens-model mass compares with the stellar mass and the abundance-matched halo mass. The lensing masses range from  $\sim 10^{11}$  to  $> 10^{13} M_{\odot}$ . Preliminary estimates of the stellar masses show a smaller spread in stellar mass (except for two lenses): a factor of a few below or above  $\sim 10^{11} M_{\odot}$ . Therefore, we expect the stellar-to-total mass fraction to decline sharply as lensing mass increases. The most massive system with a convincing model is J1434+522 (SW 05). The two low-mass outliers are J0206–095 (SW 19) and J2217+015 (SW 42); if these two are indeed lenses, they probe an interesting regime of very low star formation efficiency. Some improvements to the modelling software (SpaghettiLens), and discussion of strategies regarding scaling to future surveys with more and frequent discoveries, are included.

**Key words:** gravitational lensing: strong – galaxies: general – galaxies: stellar content – dark matter.

## 1 INTRODUCTION

By a curious coincidence, the typical escape velocity of massive galaxies – of the order of a few hundred  $\text{km s}^{-1}$  – is such that  $v_{\text{esc}}^2/c^2$ , expressed as an angular distance, is comparable to the apparent sizes of galaxies at cosmological distances. This coincidence is fortunate, because it makes the gravitational lensing deflection angle of distant galaxies ( $\alpha \sim 2v_{\text{esc}}^2/c^2$ ) comparable to their size on the sky. As a result, strong lensing by galaxies produces images that probe their host dark matter haloes, providing a useful tool to understand galaxy formation. While there is a general consensus about the basic mechanisms at play, involving gravitational collapse, fragmentation, and mergers of dark-matter clumps, into

which gas fell, cooling through radiative processes to form dense clouds and eventually stars, there is much debate about the details (for a summary, see Silk & Mamon 2012). In particular, the nature of dark matter remains mysterious: most researchers take it to be a collisionless non-relativistic fluid (cold dark matter or CDM) readily studied by simulations (for example, the influential Millennium simulation; Springel et al. 2005). However, alternative scenarios, where dark matter has exotic dynamical properties (Saxton & Ferreras 2010; Schive et al. 2016), or is not really matter at all, but a modification of gravity (McGaugh, Lelli & Schombert 2016), have also been considered.

All this motivates the use of strong gravitational lensing over galaxy scales to study the mutual dynamics of dark matter, gas and stars. Several studies in recent years have done so (see e.g. Koopmans et al. 2009; Leier et al. 2011; Leier, Ferreras & Saha 2012; Bruderer et al. 2016; Leier et al. 2016) but it is desirable to

\* E-mail: rafael.kueng@uzh.ch (RK); psaha@physik.uzh.ch (PS)

enlarge the samples from tens of lensing galaxies to thousands. Doing so requires both finding more lenses and also modelling their mass distribution. Recent searches through the CFHT Lens Survey (CFHTLS; Heymans et al. 2012) using arc-finders (e.g. More et al. 2012; Gavazzi et al. 2014; Maturi, Mizera & Seidel 2014; Sonnenfeld et al. 2017) by either machine learning methods (e.g. Paraficz et al. 2016; Lanusse et al. 2018) or visual inspection by citizen-science volunteers through the Space Warps project (More et al. 2016) have, between them, discovered an average of four lenses per square degree, so one can be optimistic about finding many thousands of lenses in the next generation of wide-field surveys, from ground-based surveys such as LSST in the optical window and SKA in radio, to space-based missions such as Euclid and WFIRST (Oguri & Marshall 2010; Collett 2015). The availability of the recently published year 1 result of the Dark Energy Survey (Drlica-Wagner et al. 2017), which covered  $1800 \text{ deg}^2$ , suggests that the number of lenses could grow by at least an order of magnitude within a very short time period.

The expected flood of new lens discoveries will need a similarly large modelling effort to reconstruct their mass distributions. Lens-modelling robots have started to be developed (Hezaveh, Perreault Levasseur & Marshall 2017; Nightingale, Dye & Massey 2017) but so far are able to handle only very clean systems. For typical lenses, human input is still needed. With that in mind Küng et al. (2015) developed a new modelling strategy, implemented as the SpaghettiLens<sup>1</sup> system. The idea is to collaborate with experienced members of the citizen-science community who have already participated in lens discovery through Space Warps, as well as several other projects involving astronomical data. The system was tested on a sample of simulated lenses, which were part of the training and testing set in Space Warps.

This paper follows up that study by applying SpaghettiLens to candidates discovered through Space Warps. We present results from the modelling of 58 of the 59 lens candidates reported by More et al. (2016). Each lens candidate was modelled following a collaborative refinement process, where anyone interested could improve the analysis by modifying an existing model or creating a new one. Note the difference with respect to the main Space Warps project, where volunteers from a group of  $\gtrsim 10^4$  people make independent contributions. Each person is presented with a random selection of survey-patches and invited to (in effect) vote on each. The system estimates the skill level of each volunteer according to test-patches interspersed with the real data, and weights their votes accordingly (Marshall et al. 2016). There is an active forum for volunteers, but since everyone is seeing different data samples with minimal overlap, the forum has little if any influence on the votes. In SpaghettiLens, the number of volunteers is significantly lower, but the level of interaction is higher. The resulting model represents a consensus among contributors, as to the best that could be achieved with the available data and software.

We emphasize that the interpretation of the results presented here is tentative, because the systems are lens candidates at this stage, not secure lenses. Moreover the candidate-lens redshifts have large uncertainties, while the candidate-source redshifts can only be guessed at present. Nevertheless it is interesting to explore the trends observed with the already available data, based on some 300 models created by eight volunteers for 58 candidate lenses found in the  $150 \text{ deg}^2$  CFHTLS.

This paper is organized as follows. Section 2 introduces the candidate lenses, their models and the diagnostics applied to them. The following sections elaborate on the diagnostics. Image morphology diagnostics are explained in Section 3 and diagnostics based on the mass models are discussed in Section 4. Stellar masses are presented in Section 5, to compare stellar and lensing masses. Finally, Section 6 summarizes and tabulates the diagnostics in Table 1.

We include three appendices devoted to various technical issues relating to the modelling. The online supplement gives the results from all the modelled systems generated for all the lensing candidates.

## 2 THE CANDIDATES AND MODELS

Space Warps is a citizen-science gravitational lens search (Marshall et al. 2016). Its first run searched the CFHT Legacy Survey, a survey carried out in five optical bands ( $u^*, g^*, r^*, i^*, z^*$ ) covering a total area of  $160 \text{ deg}^2$  divided up into four fields W1–W4. The MegaPrime camera, used for the survey, has a field of view of  $1 \text{ deg}^2$ , with  $0.186 \text{ arcsec}$  pixels. The flux limit of the survey is  $g' < 25.6 \text{ AB}$  ( $5\sigma$ ) with a typical seeing FWHM  $\sim 0.7 \text{ arcsec}$  (Erben et al. 2013). The cut-outs shown to the volunteers were colour composites of the  $g^*, r^*$  and  $i^*$  bands from randomly chosen regions. The programme resulted in 59 new lens candidates, of which 29 are considered high quality. Moreover, 82 previously known lens candidates were ‘rediscovered’. The candidates have broadly similar redshifts ( $0.2 < z < 1.0$ ), Einstein radii between 0.7 and 5 arcsec, and arc fluxes in  $g$ -band AB magnitudes between 22 and 26. These properties are similar to those found by previous robotic searches like ArcFinder and RingFinder (More et al. 2016).

A first version of SpaghettiLens was launched in 2013 May, while the first run of Space Warps was ongoing. Fig. 1 shows the total number of models generated since launch for our lens candidates. A small number of volunteers started creating models of possible lens candidates from Space Warps that were debated in the discussion forum. In the beginning of 2013 August (around day 70 since release), a modelling challenge for the candidate later to be identified as SW 01 was launched. A group of five volunteers presented their results in an online letter converging on a set of 30 models. In 2015 April (day 700), the first major version of SpaghettiLens was released. At the same time, the list of identified candidates was made available (as a preprint of More et al. 2016). At this stage, the volunteers were asked to create models for all the lens candidates that were still missing. The work done for candidate SW 29 shows that the volunteers converged on a favourable model much faster, after 15 models, generated in 30 d. The total modelling effort resulted in a set of 377 SpaghettiLens models for all but one of the 59 Space Warps lens candidates; candidate SW 39 was not modelled by any volunteer. Over its runtime, the system logged eight major contributors (defined as volunteers that generated, at least, five models).

In parallel, Küng et al. (2015) tested the system on simulated lenses and identified some areas for improvement. In Section A1, we introduce fitting of the surface brightness profile of the source. This feature has not been included yet in SpaghettiLens, but we carried the analysis during post-processing for a few interesting cases. In Section A2, we show that fine-grained mass maps within the central region relieve a tendency in the earlier work for mass profiles to be too shallow. In Section A3, we consider the possibility of fitting a parametric lens model to the ensemble.

We characterize each model with seven diagnostics, grouped into three categories, whose purpose is to help identify the most likely

<sup>1</sup> <http://labs.spacewarps.org/spaghetti/>

**Table 1.** Diagnostics of the selected models for each Space Warps candidate (see Section 6). The full table is available online.

| SWID  | ZooID       | CFHTLS name      | $z_{\text{lens}}$ | Unblended images | All images discernible | Isolated lens | Image morphology | Synthetic image reasonable | Mass map reasonable | $\log_{10} \frac{M_{\text{lens}}}{M_{\odot}}$ | $\log_{10} \frac{M_{\text{gal}}}{M_{\odot}}$ | Halo-matching index $\mathcal{H}$ |
|-------|-------------|------------------|-------------------|------------------|------------------------|---------------|------------------|----------------------------|---------------------|---|--|-----------------------------------|
| SW 01 | ASW000 4dv8 | J022409.5–105807 | –                 | x                | x                      | x             | LQ               | ✓                          | ✓                   | –   | –  | –                                 |
| SW 02 | ASW000 619d | J140522.2+574333 | 0.7               | x                | ✓                      | x             | SQ               | ✓                          | ✓                   | 11.4  | 12.4   | 0.47                              |
| SW 03 | ASW000 6mea | J142603.2+511421 | –                 | ✓                | x                      | x             | D                | ✓                          | ✓                   | –   | –  | –                                 |
| SW 04 | ASW000 9cj5 | J142934.2+562541 | 0.5               | ✓                | x                      | x             | D                | x                          | ✓                   | 11.3  | 13.1   | 0.93                              |
| SW 05 | ASW000 7k4r | J143454.4+522850 | 0.58              | ✓                | ✓                      | ✓             | IQ               | ✓                          | ✓                   | 11.3  | 13.0   | 0.83                              |
| SW 06 | ASW000 8swn | J14327.9+563832  | 0.5               | x                | ✓                      | ✓             | SQ               | ✓                          | x                   | 11.1  | 11.9   | 0.46                              |
| SW 07 | ASW000 7e08 | J20256.8+023432  | –                 | ✓                | ✓                      | x             | D                | ✓                          | ✓                   | –   | –  | –                                 |
| SW 08 | ASW000 99ed | J020648.0–065639 | 0.8               | ✓                | ✓                      | x             | D                | ✓                          | ✓                   | 11.4  | 12.3   | 0.40                              |
| SW 09 | ASW000 2asp | J020832.1–043315 | 1.0               | x                | ✓                      | ✓             | SQ               | ✓                          | ✓                   | 11.5  | 12.5   | 0.40                              |
| SW 10 | ASW000 2bmc | J020848.2–042427 | 0.8               | ✓                | x                      | ✓             | D                | x                          | x                   | 11.3  | 11.9   | 0.29                              |
| SW 11 | ASW000 2qtn | J020849.8–050429 | 0.8               | x                | ✓                      | x             | LQ               | ✓                          | ✓                   | 11.2  | 11.8   | 0.29                              |
| SW 12 | ASW000 3wsu | J022406.1–062846 | 0.4               | ✓                | ✓                      | x             | D                | ✓                          | ✓                   | 10.8  | 11.5   | 0.44                              |
| SW 13 | ASW000 47ae | J022805.6–051733 | 0.4               | x                | x                      | x             | SQ               | x                          | x                   | 11.1  | 11.9   | 0.46                              |
| SW 14 | ASW000 4xjk | J023123.2–082535 | –                 | x                | x                      | x             | SQ               | x                          | ✓                   | –   | –  | –                                 |
| SW 15 | ASW000 4nan | J084841.0–045237 | 0.3               | x                | ✓                      | x             | CQ               | ✓                          | ✓                   | 10.7  | 11.6   | 0.59                              |
| SW 16 | ASW000 9bp2 | J140030.2+574437 | 0.4               | x                | x                      | ✓             | D                | x                          | ✓                   | 11.3  | 12.1   | 0.34                              |
| SW 17 | ASW000 5rb  | J140622.9+520942 | 0.7               | ✓                | x                      | x             | D                | x                          | ✓                   | 11.1  | 12.0   | 0.44                              |
| SW 18 | ASW000 7hu2 | J143658.1+533807 | 0.7               | ✓                | x                      | ✓             | D                | x                          | x                   | 11.4  | 12.1   | 0.31                              |
| SW 19 | ASW000 11d7 | J020642.0–095157 | 0.2               | x                | ✓                      | x             | IQ               | x                          | ✓                   | 9.6   | 11.1   | 0.84                              |
| SW 20 | ASW000 2dx7 | J021221.1–105251 | 0.3               | ✓                | ✓                      | ✓             | D                | x                          | ✓                   | 11.2  | 12.0   | 0.44                              |
| SW 21 | ASW000 4m3x | J022533.3–053204 | 0.5               | ✓                | x                      | x             | D                | x                          | ✓                   | 11.1  | 11.5   | 0.24                              |
| SW 22 | ASW000 9ab8 | J022716.4–105602 | 0.4               | x                | x                      | x             | D                | x                          | ✓                   | 11.7  | 12.1   | 0.15                              |
| SW 23 | ASW000 3r61 | J023008.6–054038 | 0.6               | x                | ✓                      | x             | LQ               | x                          | ✓                   | 11.2  | 12.6   | 0.71                              |
| SW 24 | ASW000 50sk | J023315.2–042243 | 0.7               | x                | ✓                      | x             | D                | ✓                          | ✓                   | 11.4  | 11.8   | 0.19                              |
| SW 25 | ASW000 07mq | J090308.2–043252 | –                 | x                | x                      | ✓             | D                | x                          | ✓                   | –   | –  | –                                 |
| SW 26 | ASW000 5ma2 | J135755.8+571722 | 0.8               | ✓                | x                      | ✓             | D                | x                          | x                   | 11.4  | 12.3   | 0.43                              |
| SW 27 | ASW000 6jh5 | J141432.9+534004 | 0.7               | x                | x                      | x             | LQ               | x                          | ✓                   | 10.7  | 11.7   | 0.67                              |
| SW 28 | ASW000 7xrs | J143055.9+572431 | 0.7               | x                | ✓                      | x             | LQ               | ✓                          | ✓                   | 11.5  | 12.1   | 0.23                              |
| SW 29 | ASW000 8qsm | J143838.1+572647 | 0.8               | x                | ✓                      | ✓             | SQ               | ✓                          | ✓                   | 11.4  | 12.1   | 0.31                              |
| SW 30 | ASW000 2p8y | J021057.9–084450 | –                 | ✓                | x                      | x             | IQ               | x                          | x                   | –   | –  | –                                 |
| SW 31 | ASW000 21r0 | J021514.6–092440 | 0.7               | x                | ✓                      | x             | LQ               | ✓                          | ✓                   | 11.3  | 12.7   | 0.65                              |
| SW 32 | ASW000 4iye | J022359.8–083651 | –                 | x                | ✓                      | x             | IQ               | ✓                          | ✓                   | –   | –  | –                                 |
| SW 33 | ASW000 3s0m | J022745.2–062518 | 0.6               | ✓                | ✓                      | x             | D                | x                          | ✓                   | 10.9  | 12.1   | 0.77                              |
| SW 34 | ASW000 51ld | J023453.5–093032 | 0.5               | x                | x                      | ✓             | D                | x                          | ✓                   | 10.9  | 11.9   | 0.59                              |
| SW 35 | ASW000 4wgd | J084833.2–044051 | 0.8               | x                | ✓                      | x             | LQ               | ✓                          | ✓                   | 11.4  | 12.1   | 0.32                              |
| SW 36 | ASW000 096t | J090248.4–010232 | 0.4               | ✓                | ✓                      | x             | D                | x                          | ✓                   | 11.0  | 12.0   | 0.56                              |
| SW 37 | ASW000 86xq | J143100.2+564603 | –                 | x                | x                      | ✓             | SQ               | ✓                          | ✓                   | –   | –  | –                                 |
| SW 38 | ASW000 9cp0 | J143353.6+542310 | 0.8               | x                | ✓                      | ✓             | LQ               | ✓                          | ✓                   | 11.6  | 12.6   | 0.42                              |
| SW 39 | ASW000 5qiz | J202015.2+012124 | –                 | –                | –                      | –             | –                | –                          | –                   | –   | –  | –                                 |
| SW 40 | ASW000 8wmr | J221306.1+014708 | –                 | x                | ✓                      | ✓             | SQ               | ✓                          | ✓                   | –   | –  | –                                 |
| SW 41 | ASW000 8xbu | J221519.7+005758 | 0.4               | ✓                | x                      | ✓             | IQ               | ✓                          | ✓                   | 10.5  | 11.8   | 0.80                              |
| SW 42 | ASW000 96rm | J221716.5+015826 | 0.1               | ✓                | ✓                      | x             | IQ               | ✓                          | ✓                   | 8.6   | 11.0   | 1.04                              |
| SW 43 | ASW000 1c3j | J020810.7–040220 | 1.0               | x                | x                      | x             | SQ               | x                          | ✓                   | 11.6  | 12.4   | 0.34                              |
| SW 44 | ASW000 2k40 | J021021.5–093415 | 0.4               | ✓                | ✓                      | x             | LQ               | ✓                          | ✓                   | 11.3  | 12.8   | 0.76                              |
| SW 45 | ASW000 24id | J021225.2–085211 | 0.8               | x                | ✓                      | ✓             | CQ               | x                          | ✓                   | 11.7  | 12.6   | 0.37                              |
| SW 46 | ASW000 24q6 | J021317.6–084819 | 0.5               | ✓                | ✓                      | x             | D                | ✓                          | ✓                   | 10.9  | 11.8   | 0.49                              |
| SW 47 | ASW000 3r6c | J022843.0–063316 | 0.5               | ✓                | x                      | ✓             | D                | x                          | ✓                   | 11.2  | 12.6   | 0.71                              |
| SW 48 | ASW000 0g95 | J090219.0–053923 | –                 | ✓                | x                      | ✓             | D                | ✓                          | ✓                   | –   | –  | –                                 |
| SW 49 | ASW000 07ls | J090319.4–040146 | –                 | x                | ✓                      | ✓             | D                | ✓                          | ✓                   | –   | –  | –                                 |
| SW 50 | ASW000 08a0 | J090333.2–005829 | –                 | ✓                | x                      | ✓             | LQ               | ✓                          | ✓                   | –   | –  | –                                 |
| SW 51 | ASW000 6eo0 | J135724.8+561614 | –                 | ✓                | ✓                      | x             | D                | x                          | ✓                   | –   | –  | –                                 |
| SW 52 | ASW000 6a07 | J140027.9+541028 | –                 | ✓                | x                      | ✓             | SQ               | ✓                          | ✓                   | –   | –  | –                                 |
| SW 53 | ASW000 70vl | J141518.9+513915 | 0.4               | ✓                | x                      | ✓             | D                | x                          | ✓                   | 11.3  | 12.5   | 0.56                              |
| SW 54 | ASW000 7sez | J142620.8+561356 | 0.5               | x                | ✓                      | x             | CQ               | ✓                          | ✓                   | 11.1  | 12.3   | 0.68                              |
| SW 55 | ASW000 7t5y | J142652.8+560001 | –                 | x                | ✓                      | ✓             | CQ               | ✓                          | x                   | –   | –  | –                                 |
| SW 56 | ASW000 7pga | J142843.5+543713 | 0.4               | ✓                | x                      | ✓             | D                | x                          | x                   | 10.7  | 12.0   | 0.80                              |
| SW 57 | ASW000 8pag | J143631.5+571131 | 0.7               | x                | ✓                      | x             | SQ               | x                          | x                   | 10.9  | 12.7   | 1.08                              |
| SW 58 | ASW000 7iwp | J143651.6+530705 | 0.6               | x                | x                      | ✓             | LQ               | ✓                          | ✓                   | 11.4  | 12.6   | 0.58                              |
| SW 59 | ASW000 85cp | J143950.6+544606 | –                 | ✓                | x                      | ✓             | D                | ✓                          | ✓                   | –   | –  | –                                 |

cases of a gravitational lens, as well as flag the most interesting candidates for future follow-up observations. The diagnostics are as follows.

(i) First, we have diagnostics based on morphology. Section 3 and Fig. 2 explain this diagnostic in more detail. We consider:

(a) Whether the images are unblended: Distinct, unblended images are an advantage in modelling, although not essential.

(b) Whether all images are discernible. The topography of an arrival-time surface, as encoded by a spaghetti diagram, may require more images than are visible, in which case the modeller has to insert conjectural image positions.

(c) Whether the lens is isolated.

(d) The image morphology concisely described: double or quads, further sub-categorized to indicate the elongation direction of the lensing mass.

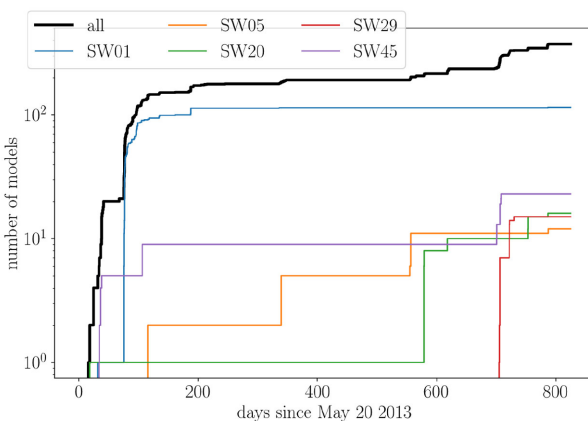


**Figure 1.** Number of models generated over time in days since the launch of SpaghettiLens; the black line shows all models, and the coloured lines show the five most active candidates. A total of 377 models were generated for 58 lens candidates, eight users contributed more than five models per person.

(ii) Secondly, we have mass models, covered in Section 4. We assess the following points:

(e) Whether the mass map is reasonable (see Fig. 5).  
(f) Whether the arrival-time surface and synthetic image are plausible. In particular, an unsatisfactory model is flagged when additional images are implied in regions where they are not observed (see Figs 3, 4 and 6).

(iii) Thirdly, whether the total implied lensing mass determined from the lens model is plausible, given the photometry of the lensing galaxy. In this work, we define the lensing mass as the sum of all mass tiles in the model. These mass tiles reach out to typically twice the radius of the outermost image. Section 5 explains how we compare the lensing mass with the stellar mass. Galaxies may have haloes extending well beyond the mass maps in the models, so the calculated lensing mass is only a lower bound on the total galaxy mass. Hence, the lensing mass should be somewhere between the stellar mass (lower bound) and the total halo mass (upper bound). Extrapolation of the lens model to estimate the full virial mass may be possible (cf. Leier et al. 2012), but is not attempted in this work.

(g) We then introduce a so-called halo index ( $\mathcal{H}$ ), which quantifies how the lensing mass compares with these two constraints (see Fig. 7).

### 3 IMAGE MORPHOLOGY

The main input of a modeller to the process is a markup of the candidate lens system, which we call a spaghetti diagram. This is a sketch of the arrival-time surface from a point-like source, with proposed locations of maxima, minima and saddle points, and an implied time-ordering of the images. Such information encodes a starting proposal for the mass distribution. A spaghetti diagram is thus a completely abstract construction, and moreover it refers to a simplified system with a point source. However, spaghetti diagrams are intuitive because they tend to resemble the form of lensed arcs (see fig. 3 of Ferreras, Saha & Burles 2008), and of course they are simple to draw, and easy to vary and refine in an open collaborative environment. This makes them very practical for non-professional lens enthusiasts in the citizen-science community. Details and tests are given in Küng et al. (2015).

We now discuss the diagnostics that can be taken from the process of drawing the spaghetti diagram, even before detailed mass-modelling takes place. Fig. 2 shows nine examples, each consisting of a cut-out of the Space Warps image of a lens candidate, marked up with a spaghetti diagram. The volunteers are initially presented a square image with side 82 arcsec (440 pixels) in full size, but they have the ability to zoom in individually. The cut-outs presented in Figs 2–5 are rescaled during post-processing, relative to the outermost image.

All the examples shown in Fig. 2 identify five locations: the centre of the main lensing galaxy, which is also a maximum of the arrival-time surface (red dots); two minima (blue dots); and two saddle points (green dots and also self-intersections of the curves). Only two (SW 05 and SW 42) of the nine systems, however, have five distinct features in plausible locations. In the other seven examples, an arc is interpreted as a blend of three or four images. This defines the ‘unblended images’ diagnostic. Note that this characterization could be different if the spaghetti diagram were different. For example, SW 28 has also been modelled with the arc on the right interpreted as a single image, rather than as three images as shown in the figure; for such a model, the ‘unblended images’ diagnostic would be true.

The second diagnostic checks whether all images are visible. For example, we see in SW 58 at the top left of Fig. 2 that an image at the second minimum is conjectural and does not correspond to any visible feature.

The third diagnostic tests whether the lens is isolated, or whether other galaxies could contribute to the lensing, based on visual inspection of the field. For this, we do not consider stars or other clearly foreground objects. Additional galaxies contributing to the lensing mass can be marked by the volunteer alongside the spaghetti diagrams. An example can be seen as the grey dot and circle in the cut-out with SW 57 at the top right of Fig. 2. Objects marked in this way are modelled as point masses. Other possible contributors to lensing are galaxies or groups that are not in the immediate vicinity of the lensed images, yet massive enough to exert an influence. These are accounted for by allowing a constant but adjustable external shear.

We remark that the lack of expected lensed images, or the presence of blended images or perturbing galaxies, does not imply that a given candidate is unlikely to be a lens. This means, rather, that the models are more uncertain and perhaps could be more easily improved by trying further variations in the markup.

The fourth diagnostic is based on the fact that the arrangement of lensed images of a point-like source through non-circular gravitational lens depends on the location of the source relative to the long and short axes of the lens. This dependence is quite robust and independent of many other details of the lensing mass distribution. Sources close to being dead-centre behind a lens tend to produce quads; sources at larger transverse distance tend to produce doubles. We denote these as Q and D, respectively, and add a prefix to the Q systems as follows: we write LQ if the source is inferred as displaced along the long axis of the lens, SQ if displaced along the short axis, IQ if inclined to both axes, and CQ if only very little or no displacement is evident. Although the unlensed source and its location are obviously not seen, the LQ, SQ, IQ and CQ cases correspond to easily seen image morphologies (see e.g. Saha & Williams 2003).

(i) The simplest is the LQ case: this creates a saddle point and two minima in an arc, with the second saddle point on the other side of the lensing galaxy, closer to the galaxy than the arc. SW 58 and

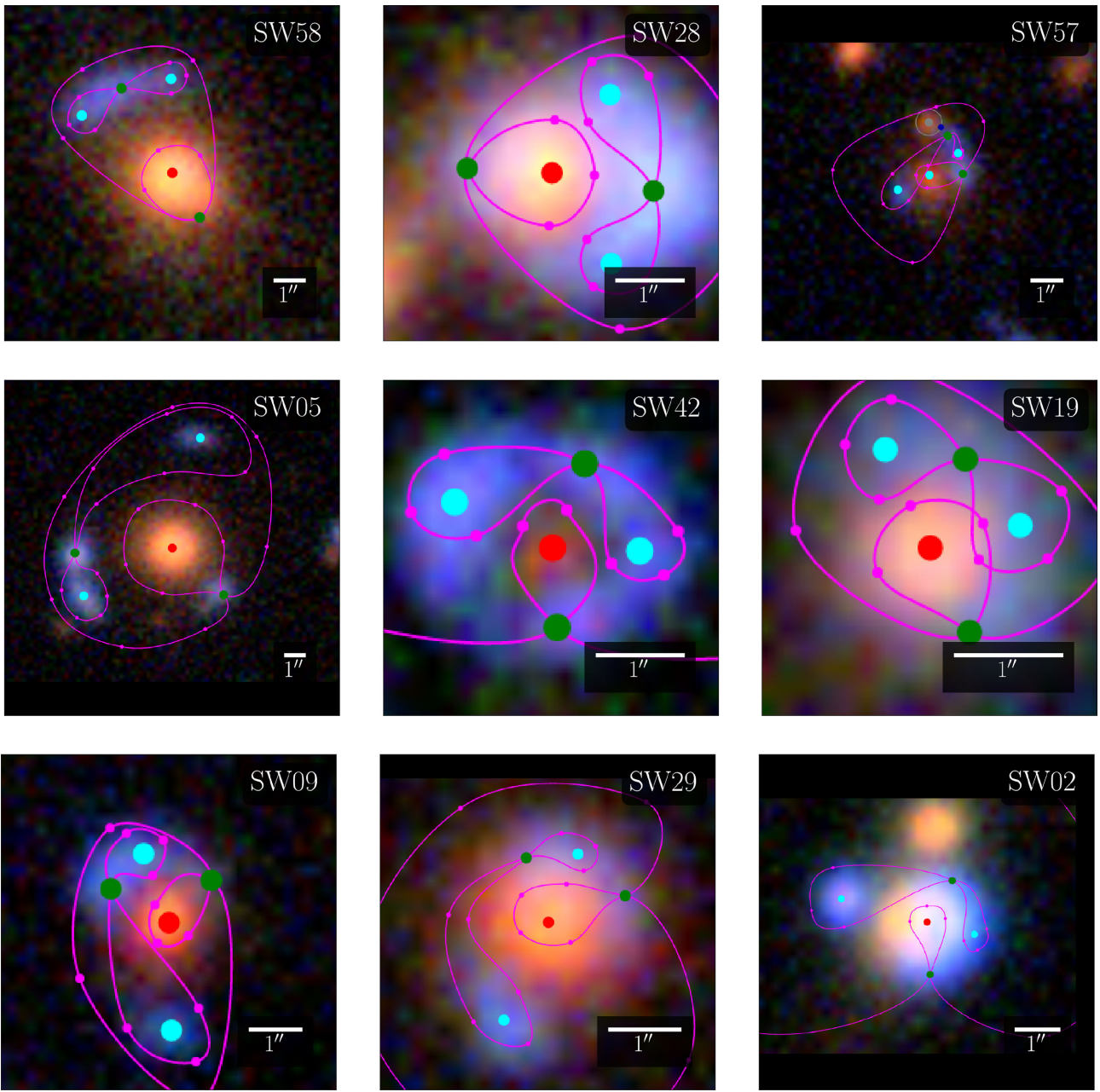


**Figure 2.** Nine of the lens candidates marked up with spaghetti diagrams. Red, blue and green dots are proposed locations for maxima, minima and saddle points of the arrival time, respectively. The curves help guide the placement of the dots, but their precise appearance has no significance. These images are screenshots from the SpaghettiLens user interface, which applies interpolation to background images. The scaling is adjusted to fit the other images. This selection includes the best-modelled systems, but also one case (SW 57 at upper right) of unsuccessful modelling. Since the modelling process is collaborative among the volunteers, with anyone welcome to contribute new models or modify existing ones, there are variant spaghetti diagrams for all the modelled systems. The online supplement displays all the models presented for discussion during this work.

SW 28 in the upper row of Fig. 2 are typical examples of LQ. If the source were moved outwards along the short axis, the minimum-saddle-minimum set would merge into a single minimum, leaving a D system; the transition is known as a cusp catastrophe.

(ii) The middle row of Fig. 2 shows three IQ systems: SW 05, SW 42 and SW 19. This type has a characteristic asymmetry, often with two images close together. If the source were moved outwards, the minimum-saddle pair would merge and mutually cancel, leaving again a D system. This transition is known as a fold catastrophe.

(iii) The lower row of Fig. 2 shows three SQ systems: SW 09, SW 29 and SW 02. The failed model, SW 57, at top right may also belong to this category. Here, the images have a fairly symmetric arrangement with an arc and a counter-image on the other side, but the spaghetti diagram is completely asymmetric. If the source were moved outwards along the long axis, the saddle-minimum-saddle set would merge into a single saddle – another form of cusp catastrophe. SQ can be visually distinguished from LQ by the relative distances of the arc and the counter-image. For SQ, the arc is closer, and for LQ the counter-image is closer.

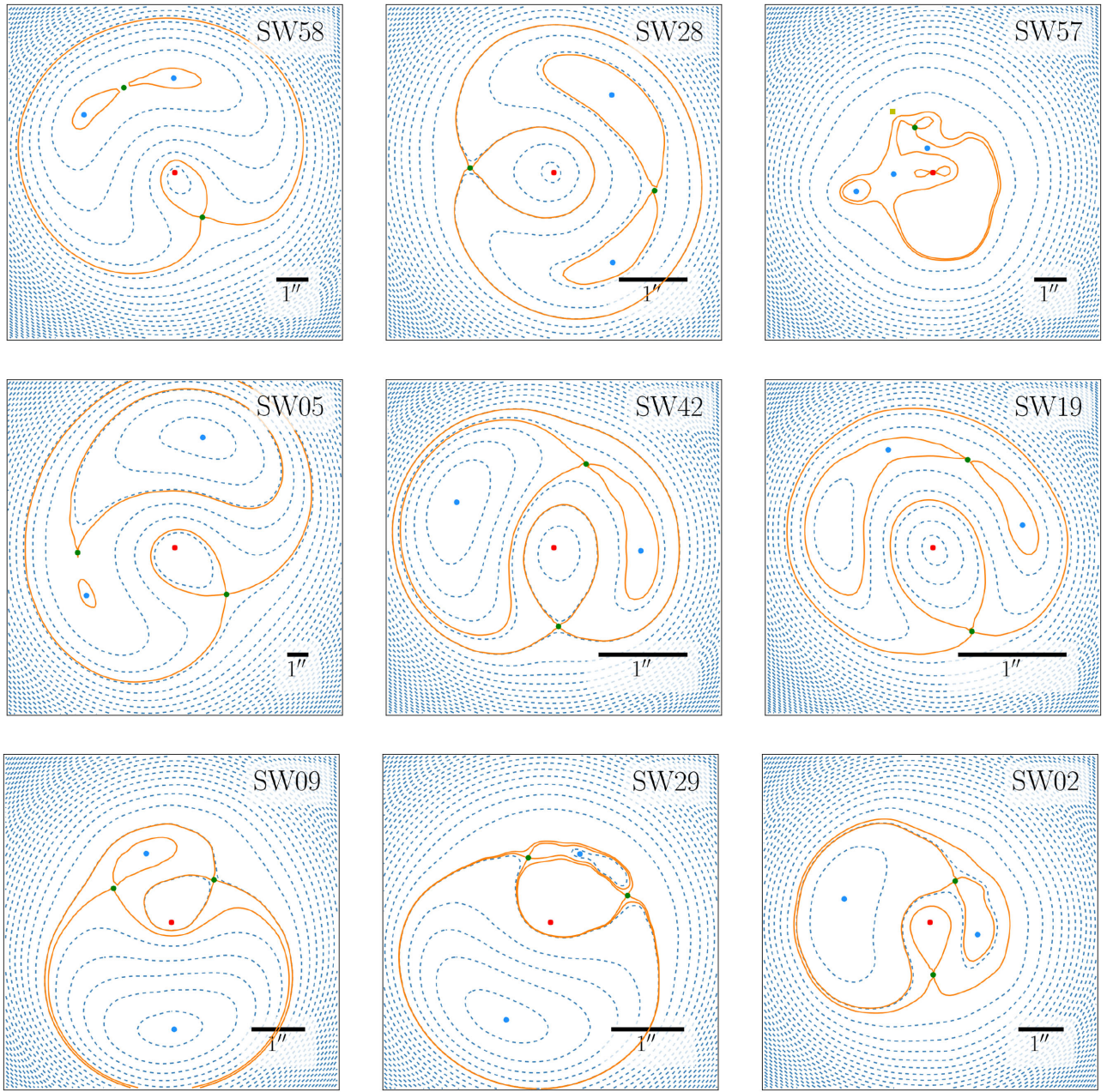


**Figure 3.** Arrival-time surfaces for models of the systems from Fig. 2. The registration differs slightly from Fig. 2, but the coloured dots represent exactly the sky positions specified in the earlier figure. The orange contours only qualitatively resemble the earlier pink curves, as they are now precise saddle-point contours from lens models.

CQ systems are often called ‘cross’ or ‘Einstein-cross’ systems; IQ systems are sometimes called ‘folds’, with ‘cusp’ commonly used for both SQ and LQ. The labels ‘short-axis quad’ and so on are not standard in the literature, but the morphological classification they express is familiar to experienced modellers. Hence, they can be useful to researchers wishing to apply other modelling methods to the same systems.

#### 4 MASS MODELS

Once a spaghetti diagram has been drawn on a web browser, it is forwarded to a server-side numerical framework, which searches for mass maps consistent with the image locations, parities and time

ordering, given by the modeller. The mass maps are made up of mass tiles and are free-form, but are required to be concentrated around the identified lens centre (see Coles, Read & Saha 2014, for the precise formulation of the search problem). The modeller can also set various options for the search, such as the number of mass tiles and the extent of the mass map; all options have defaults. Typically, there are  $\sim 500$  mass tiles arranged in a disc, centred on the lensing galaxy and extending to twice the radius of the outermost image. By default, the mass distributed is required to have a  $180^\circ$ -rotation symmetry, but this option can be unset. Assuming mass distributions can be found, which in practice is usually the case, a statistical ensemble of 200 two-dimensional mass maps is returned. From each mass map, further quantities such as lens potentials

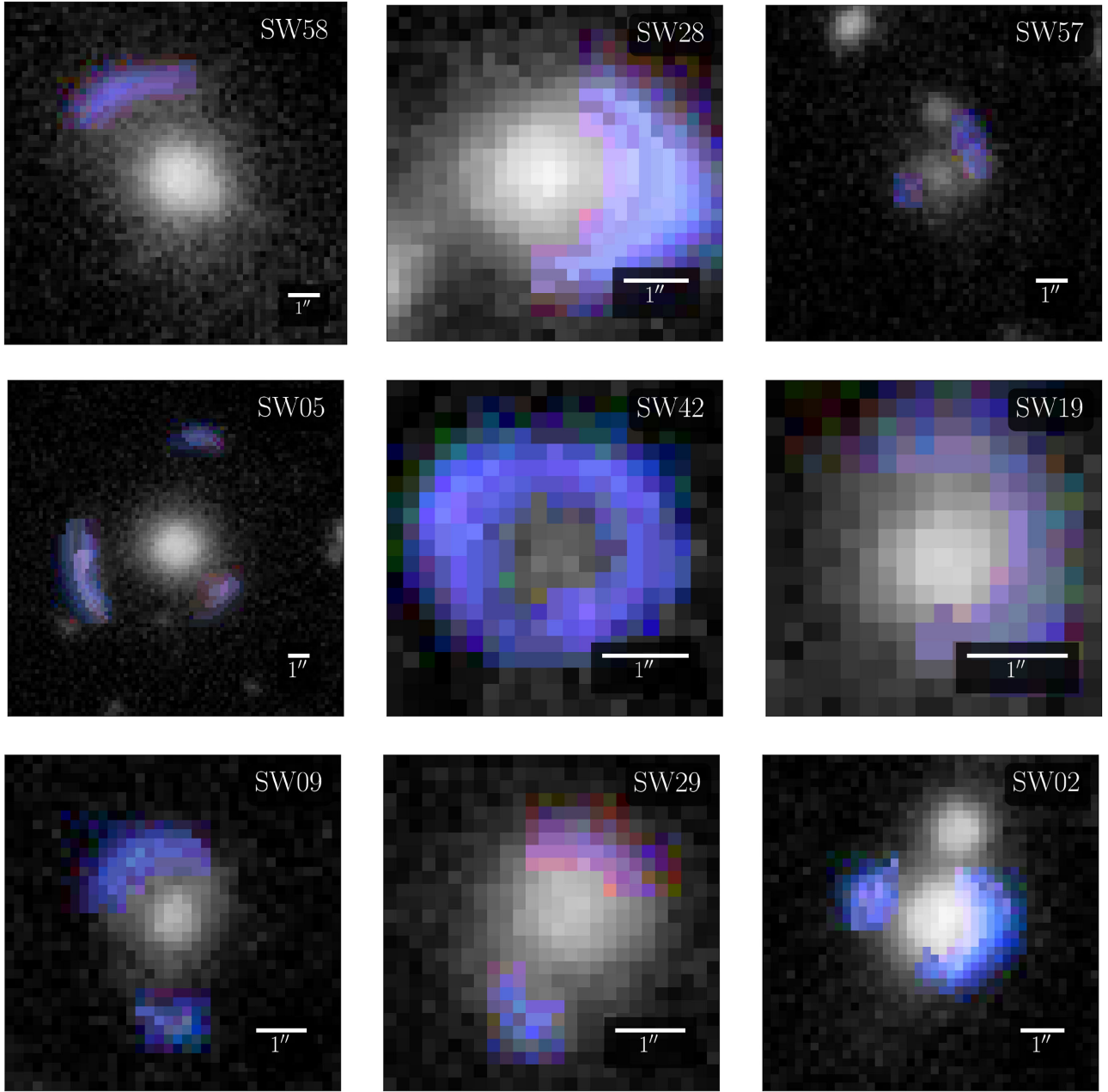


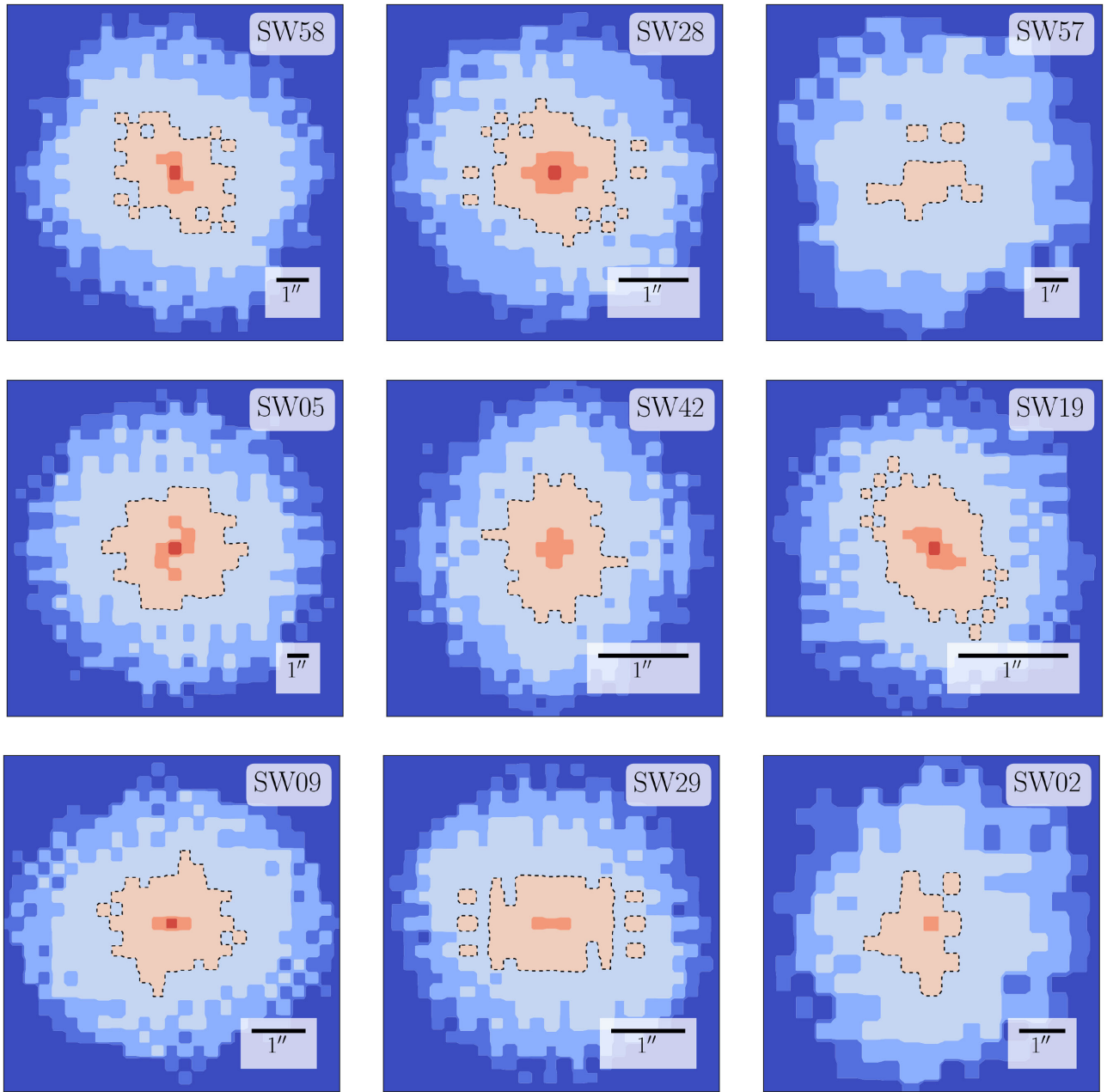
**Figure 4.** Synthetic images of the systems from Fig. 2, derived from the lens models. The reconstructed lensed features keep the Space Warps false-colour scheme from Fig. 2. The rest has been changed to black and white.

or enclosed masses can be derived. Thus, there are ensembles of 200 values for the surface density at any point, for the enclosed mass within a given radius and so on. In this paper, we present the averages and ranges of different quantities, but other quantities such as 90 per cent confidence ranges could also be computed. The whole ensemble of mass maps, along with derived quantities and uncertainties, makes up one SpaghettiLens model.

The mass will naturally depend on the lens and source redshifts, which are unknown when a lens candidate is first identified. However, this is not a problem, because a model can be trivially rescaled to use better redshift values, as they become available. The mass normalization of the models is proportional, through the angular critical density, to the factor  $d_L d_S d_{LS}^{-1}$ , where  $d_L$ ,  $d_S$  and  $d_{LS}$  are the usual angular-diameter distances. In the redshift ranges typical

of galaxy lensing, the normalization factor is roughly proportional to the lens redshift, and weakly dependent on the source redshift. This work applies photometric redshifts from the CFHTLS pipeline (Coupon et al. 2009) to the candidate lensing galaxies; the values range from  $z = 0.2$  to 1 (see Table 1). The source redshifts are assumed as  $z = 2$ , unless an unambiguous photometric redshift is available. The lens redshifts entail rather big uncertainties, up to a few tens of per cent (see fig. 5 in Coupon et al. 2009). The lensing masses would be uncertain at the same level. On the other hand, the lensing masses in the sample range from  $10^{11}$  to  $10^{13} M_\odot$ ; in comparison, the redshift uncertainty is not so important in this preliminary analysis.

The ensemble of mass maps can be post-processed in many different ways. Four different graphical quantities are particularly useful.



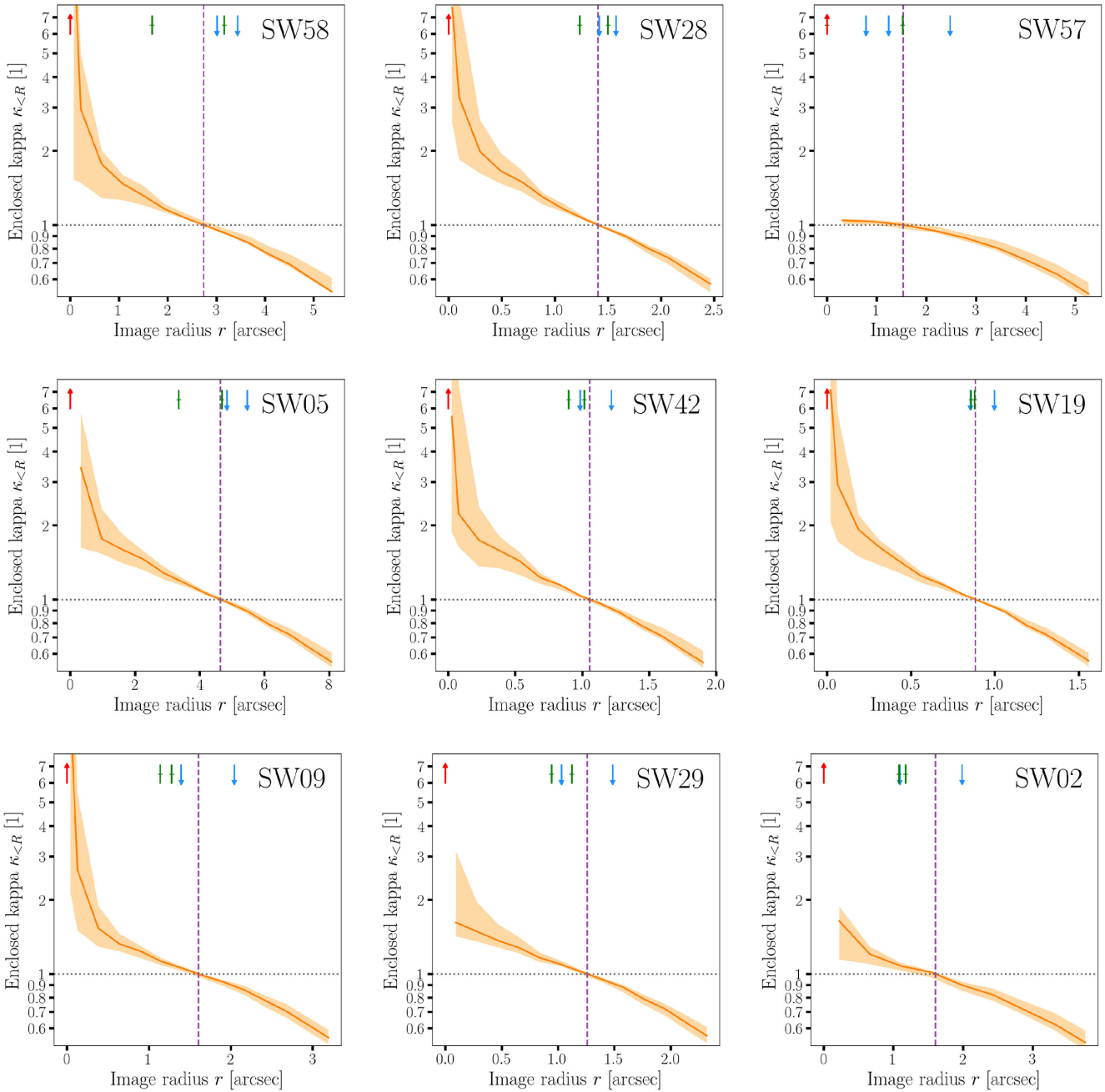
**Figure 5.** Ensemble-average mass distribution  $\kappa$  for which the results Figs 3–4 were derived. The dashed curves denote  $\kappa = 1$ . Most of the mass maps have a  $180^\circ$ -rotation symmetry, which is imposed by default. For SW 02 and SW 57, where the lensing mass is clearly asymmetric, the modeller chose to turn off the symmetry.

Fig. 3 shows the arrival-time surfaces corresponding to the spaghetti diagrams of Fig. 2. The arrival-time contours look like machine-made elaborations of the input spaghetti diagrams. If the saddle-point contours in the arrival time are qualitatively the same as the curves in the spaghetti diagram (the detailed shape of the spaghetti curves is unimportant), it immediately suggests a successful model. On the other hand, if the arrival-time surface has unexpected minima or saddle points, and especially if the unexpected features are far from identified lens images, that signals an improbable model. Fig. 4 shows what we call synthetic images, meaning reconstructions of the extended lensed features by fitting for a source. These were generated by a new method, explained in Appendix A1, implemented during the offline post-processing after

the modelling process was complete. The synthetic images provided by SpaghettiLens during the collaborative modelling and discussion were more crude; those are included in the online supplement.

The arrival-time surface and synthetic image are summarized by one diagnostic, the most important of all: are the lensed features satisfactorily reproduced? This diagnostic remains a judgment call by modellers. A useful quantitative criterion for whether the synthetic image is consistent with the data would need to allow for PSF dependence and unmodelled substructure – otherwise all models would be summarily rejected, something left for a future implementation in SpaghettiLens.

Fig. 5 shows the projected mass maps of the sample. In fact, this figure only shows the ensemble-average mass maps, and not



**Figure 6.** Cumulative circular averages of the mass maps from Fig. 5, with uncertainties. More precisely, we show the enclosed mass within a given projected radius, expressed as the mean  $\kappa$  with a given number of arcsec from the centre of the lensing galaxy. The orange bands refer to the full ensemble of mass maps for the models, while the red curves show the ensemble averages. The dashed vertical line indicates the notional Einstein radius, or where the mean enclosed  $\kappa$  is unity. The short vertical arrows mark the positions of the images (maxima, saddle points and minima).

the variation within the ensemble, from which uncertainties can be inferred. The same applies to the arrival-time surfaces and synthetic images in the previous two figures. The uncertainties will be shown in a concise form in Fig. 6. Fig. 5 makes evident the tiled nature of the mass model. The tiles can be smoothed over by interpolation, and this was done in the mass maps during the modelling process, available in the online version. It is interesting, however, to note the tiling artefacts, if only as a reminder that the substructure in the mass distribution is very uncertain, even if some integrated quantities are well constrained. How the free-form mass maps relate to parametrized lens models is discussed in Appendix A3. Note that

although the mass distribution can have discontinuous jumps, the lens equation and arrival-time surface are continuous.

Fig. 6 shows the enclosed-mass profiles, expressed as the average convergence,  $\kappa$ , within circles of a given projected radius. Uncertainties are included (see the figure caption for details). Appendix A2 describes the improvements made since our earlier work (Küng et al. 2015), to allow for steeper profiles in the inner regions. The enclosed mass is typically best constrained at the notional Einstein radius, becoming more uncertain at larger and smaller radii.

The mass maps and mass profiles are the basis of a further diagnostic: are the mass distributions plausible? This is also a judgment

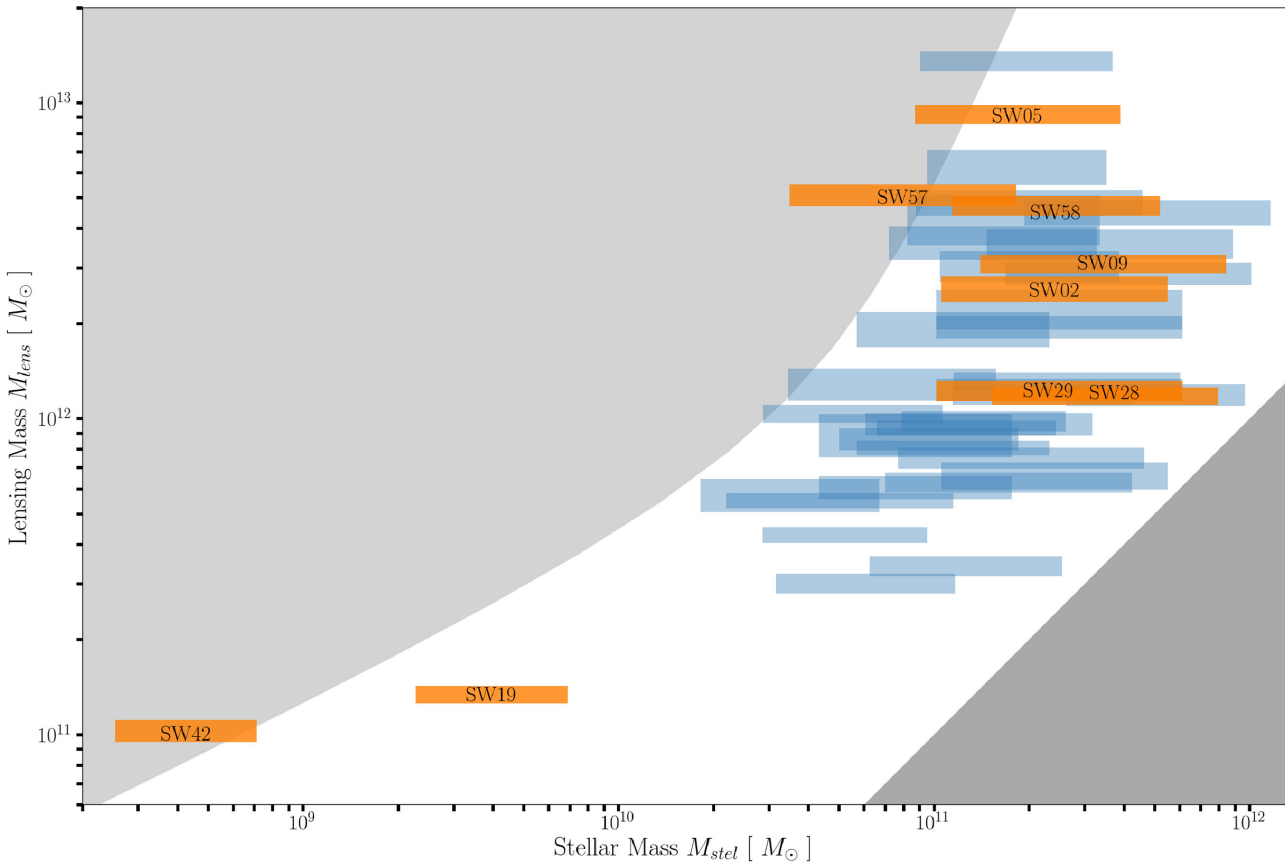


**Figure 7.** Total mass in the model against the estimated stellar mass, alongside the values for the whole sample. (The labelled orange bars are the systems shown in detail in Figs 2–6.) The horizontal extent of each bar indicates the extreme cases of a young (0.5 Gyr-old) stellar population and the oldest possible population at the given redshift. The vertical extent indicates the spread of masses in the lens-model ensemble. The lower-right shaded region is unphysical according to the stellar-population models, because it gives  $M < M_{stel}$ . The upper-left shaded region is unphysical according to abundance matching (see Section 5) because it gives  $M > M_{halo}$ . That is to say, the unshaded region is  $0 < \mathcal{H} < 1$ .

call made by modellers, but it showed to be a powerful diagnostic, summarizing three aspects. The overall shape is forced to be 180°-rotation symmetric, usually a plausible assumption, but volunteers can deactivate this constraint. The profile slope turned out to be a good indicator of plausible models, as can seen by contrasting the model for SW 57 with the rest of the sample: The missing core in Fig. 5 and the flat profile in Fig. 6 disqualify this model. The clumpiness of the mass map is another useful indicator. Flat profile slopes can often be identified directly in the mass map, where the mass tiles form a checkerboard pattern.

More experienced volunteers applied these diagnostics already during the process of creating models as a criteria of a successful model, the evaluation presented in this work however was generated by the authors during post-processing.

## 5 STELLAR AND HALO MASS ESTIMATES

The stellar masses of the lens galaxies are derived by a comparison of the photometric data with stellar  $M/L$  estimates from population synthesis models. In principle, a detailed analysis of the spectral energy distribution is needed to derive accurate stellar masses (e.g. Gallazzi & Bell 2009; Taylor et al. 2011). However, at the redshifts probed, the photometric data mainly constrain the information-rich 4000 Å break region, whose strength depends sensitively on age and metallicity, thereby providing a strong constraint on the stellar

$M/L$ . Hence, estimates to within ∼0.3 dex in  $\log(M_{stel}/M_{\odot})$  can be derived with a single colour, preferably tracing a rest-frame colour similar to  $U - V$  (see fig. 1 of Ferreras et al. 2008), assuming a universal initial mass function (IMF). There is evidence from detailed absorption line strength analysis that massive galaxies can feature a non-standard IMF (e.g. Ferreras et al. 2013). However, these variations, towards a bottom-heavy distribution, are typically found in the cores of massive early-type galaxies (La Barbera et al. 2016). The effect of these variations on the stellar  $M/L$  of lensing systems is still rather controversial (Smith, Lucey & Conroy 2015; Leier et al. 2016).

In this paper, we further simplify the analysis by assuming a relationship between the apparent total magnitude and stellar mass, at the redshift of the lens. For typical stellar-population parameters, the variation of this relation is at most  $\Delta \log M_s \sim 1$  dex. A further potential systematic can arise from contamination of the light of the lensing galaxy by the lensed background source. Reducing or eliminating the latter would require detailed fitting of light distributions for each candidate (see Leier et al. 2011), which we have not yet attempted. Nonetheless, because the lensing masses range over two orders of magnitude, it is still interesting to compare them with rough estimates of stellar mass.

We make use of the Bruzual & Charlot (2003) models to derive two functional forms of the stellar mass with respect to the  $i'$ -band magnitudes. The models have solar metallicity, with a Chabrier

IMF, and assume two different age trends: a ‘young’ model, with a constant 500 Myr age at all redshifts, and an ‘old’ model where the age is the oldest one possible at each redshift, adopting a standard  $\Lambda$ CDM model with  $H_0 = 70 \text{ km s}^{-1} \text{ Mpc}^{-1}$  and  $\Omega_m = 0.3$ .

Fig. 7 shows a comparison of stellar and lensing mass in our sample. The comparatively large span of the error bars in stellar mass (horizontal axis) shows the range between the masses derived using the two age trends, respectively, and lies between 0.4 and 0.8 dex. It will be improved in future work by the use of available optical and NIR magnitudes to derive more accurate constraints on the stellar populations. In addition, we also derive halo masses for the lenses using an abundance-matching formula. This technique matches the distribution function of observed stellar mass in galaxies with that of dark-halo masses from  $N$ -body simulations, to define a simple relation between stellar mass and halo mass. We emphasize that a halo mass from abundance matching should be considered an ‘average’ estimate, and a significant scatter can be expected as galaxies with the same stellar mass can be found in different environments. We refer the reader to Leier et al. (2012) for an assessment of the effect of abundance matching on the derivation of dark matter halo properties in lensing galaxies. We follow the prescription of Moster et al. (2010), namely:

$$\frac{M_{\text{stel}}}{M_{\text{halo}}} = \frac{2C_0}{(M_{\text{halo}}/M_1)^{-\beta} + (M_{\text{halo}}/M_1)^\gamma} \quad (1)$$

$$C_0 = 0.02820, M_1 = 10^{11.884} \text{ M}_\odot$$

$$\beta = 1.057, \gamma = 0.556.$$

Fig. 7 may be compared with Fig. 4 in More et al. (2011). The comparison of lensing and stellar mass produces the last of our model diagnostics, defined as a halo-matching index:

$$\mathcal{H} \equiv \frac{\ln(M/M_{\text{stel}})}{\ln(M_{\text{halo}}/M_{\text{stel}})} \quad (2)$$

that relates the observed lensing to stellar mass, with the global ratio expected if the host halo corresponds to the average value derived by abundance matching. Several cases for  $\mathcal{H}$  can be considered:

- (i)  $\mathcal{H} < 0$  is unphysical because  $M < M_{\text{stel}}$ .
- (ii)  $\mathcal{H} = 0$  means the stellar mass exactly accounts for the lensing mass (i.e. no dark matter affects the lensing model).
- (iii)  $0 < \mathcal{H} < 1$  is the typical situation, where the lens includes stars and dark matter, but not the full halo.
- (iv)  $\mathcal{H} = 1$  means that the lens consists of the entire halo.
- (v)  $\mathcal{H} > 1$  is in tension with abundance matching, because the lensing mass exceeds the expected halo mass.

The halo-matching index expresses whether the lensing mass is plausible given the flux received from the candidate lensing galaxy.

Fig. 7 and Table 1 show that most of the candidates have stellar and lensing masses typical of massive ellipticals.<sup>2</sup> SW05 is one of the most massive of all the candidates, corresponding to a galaxy-group mass scale. It is a particularly attractive system for follow-up observations at higher resolution, as it is a large system with clear multiple-image features. Modelling leaves little doubt that it is a lens. SW04 seems to be even more massive, but the diagnostics leave some doubts about the validity of this model. The two lowest mass systems, SW19 and SW42, are important if they are indeed lenses, as they would be low-mass lenses dominated by dark matter.

<sup>2</sup> The mass values themselves are given in the online version of Table 1.

All the modelled systems have reasonable stellar-mass fractions, except for two cases where the stellar-mass fraction is too low ( $\mathcal{H} > 1$ ): these are SW42 and SW57. In the case of SW57, the model has poor diagnostics and should be discarded. The model for SW42, on the other hand, is quite convincing – except for the high halo-matching index. If SW42 turned out not to be a lens, that would support the halo-matching index as an effective criterion to discriminate models.

## 6 SUMMARY AND CONCLUSIONS

We report on a first set of mass distributions and follow-up diagnostics for the Space Warps lens candidates created with a novel approach that aims to be scalable by *orders of magnitude* to prepare for the many thousands of lenses the next generation of wide-field surveys will yield (e.g. Euclid andWFIRST).

Over the past few years, the way of discovering lenses has changed with the introduction of machine learning and citizen-science methods, combined with the coverage of large areas of the sky by modern surveys. The way lensing mass models are constructed also needs to change, in order to be prepared for the increasing influx of lens candidates. The work in this paper represents a hybrid approach between the classical style, where a small team of experts invests many hours into the creation of a single model, and a citizen-science project, where a crowd of amateur volunteers makes independent contributions. The authors of this paper are a collaboration of professionals and experienced citizen-science volunteers, aiming to create early-stage lens models as soon as a lens candidate is found.

To assist volunteers in constraining lensing models, we introduce a set of diagnostics that helps us to assess the validity of the models. At a later stage, we encourage modellers to apply those diagnostics as feedback on the plausibility of their assumptions, and to suggest additional diagnostics.

The diagnostics (i)–(iv) (see Section 2) turned out to be useful measures of the difficulty in modelling a system, but they did not constitute necessary conditions for a promising model. They can help select systems to introduce novice volunteers to the modelling process. In contrast, diagnostics (v) and (vi) can be considered as necessary criteria for a good model. Volunteers employed those ones to evaluate their models, and turned out to be easy enough to grasp by new volunteers. The halo-matching index diagnostic (vii,  $\mathcal{H}$ ) is an interesting criterion that might be useful for the modellers, but needs further investigation.

Table 1 is a summary of our results. It characterizes each modelled system with seven diagnostics, indicating (a) the image morphology and how clear or indistinct it is, (b) whether the mass map and synthetic lensed image appear to be plausible, and (c) how the model mass compares with the estimated stellar and full-halo masses. Missing entries are due unavailable imaging data, whereas missing rows are due to models that were not created for this particular candidate.

The trend in Fig. 7, where higher-mass galaxies get progressively more dark-matter dominated, is expected (see e.g. Ferreras, Saha & Williams 2005), as is the span of about one order of magnitude for the stellar mass and the two orders of magnitude in lensing mass. With future data, it will be interesting to compare the enclosed stellar and lensing mass as a function of radius, going from the star-dominated inner regions to the outer dark haloes. Leier et al. (2011) illustrate this behaviour in their fig. 5, but the present sample could go an order of magnitude higher in mass.

The quick creation of many models for the Space Warps candidates successfully showed that a subset of citizen scientists is interested in being involved in more challenging tasks that take some time to learn. The next step involves recruiting more lensing enthusiasts, as soon as the next round of Space Warps is started. In the meantime, the improvements shown in the appendix will be integrated in the standard version of SpaghettiLens. Photometric fitting could also be integrated into SpaghettiLens. This would allow experienced citizen scientists to generate photometric redshifts and stellar masses, and thus generate preliminary dark-matter maps as soon as a lens candidate is identified.

## ACKNOWLEDGEMENTS

This work was supported by the University of Zurich Candoc research grant (Forschungskredit Candoc; FK-14-081 and FK-15-087).

## REFERENCES

- Bruderer C., Read J. I., Coles J. P., Leier D., Falco E. E., Ferreras I., Saha P., 2016, MNRAS, 456, 870  
 Bruzual G., Charlot S., 2003, MNRAS, 344, 1000  
 Coles J. P., Read J. I., Saha P., 2014, MNRAS, 445, 2181  
 Collett T. E., 2015, ApJ, 811, 20  
 Coupon J. et al., 2009, A&A, 500, 981  
 Drlica-Wagner A. et al., 2017, ApJS, preprint ([arXiv:1708.01531](https://arxiv.org/abs/1708.01531))  
 Erben T. et al., 2013, MNRAS, 433, 2545  
 Ferreras I., Saha P., Williams L. L. R., 2005, ApJ, 623, L5  
 Ferreras I., Saha P., Burles S., 2008, MNRAS, 383, 857  
 Ferreras I., La Barbera F., de la Rosa I. G., Vazdekis A., de Carvalho R. R., Falcón-Barroso J., Ricciardelli E., 2013, MNRAS, 429, L15  
 Gallazzi A., Bell E. F., 2009, ApJS, 185, 253  
 Gavazzi R., Marshall P. J., Treu T., Sonnenfeld A., 2014, ApJ, 785, 144  
 Heymans C. et al., 2012, MNRAS, 427, 146  
 Hezaveh Y. D., Perreault Levasseur L., Marshall P. J., 2017, Nature, 548, 555  
 Keeton C. R., 2001, preprint ([arXiv:astro-ph/0102341](https://arxiv.org/abs/astro-ph/0102341))  
 Koopmans L. V. E. et al., 2009, ApJ, 703, L51  
 Küng R. et al., 2015, MNRAS, 447, 2170  
 La Barbera F., Vazdekis A., Ferreras I., Pasquali A., Cappellari M., Martín-Navarro I., Schönebeck F., Falcón-Barroso J., 2016, MNRAS, 457, 1468  
 Lanusse F., Ma Q., Li N., Collett T. E., Li C.-L., Ravanbakhsh S., Mandelbaum R., Poczos B., 2018, MNRAS, 473, 3895  
 Leier D., Ferreras I., Saha P., Falco E. E., 2011, ApJ, 740, 97  
 Leier D., Ferreras I., Saha P., 2012, MNRAS, 424, 104  
 Leier D., Ferreras I., Saha P., Charlton S., Bruzual G., La Barbera F., 2016, MNRAS, 459, 3677  
 Marshall P. J. et al., 2016, MNRAS, 455, 1171  
 Maturi M., Mizera S., Seidel G., 2014, A&A, 567, A111  
 McGaugh S. S., Lelli F., Schombert J. M., 2016, Phys. Rev. Lett., 117, 201101  
 More A., Jahnke K., More S., Gallazzi A., Bell E. F., Barden M., Häußler B., 2011, ApJ, 734, 69  
 More A., Cabanac R., More S., Alard C., Limousin M., Kneib J.-P., Gavazzi R., Motta V., 2012, ApJ, 749, 38  
 More A. et al., 2016, MNRAS, 455, 1191  
 Moster B. P., Somerville R. S., Maulbetsch C., van den Bosch F. C., Macciò A. V., Naab T., Oser L., 2010, ApJ, 710, 903  
 Nightingale J., Dye S., Massey R., 2017, MNRAS, preprint ([arXiv:1708.07377](https://arxiv.org/abs/1708.07377))  
 Oguri M., Marshall P. J., 2010, MNRAS, 405, 2579  
 Paraficz D. et al., 2016, A&A, 592, A75  
 Saha P., Williams L. L. R., 2003, AJ, 125, 2769  
 Saxton C. J., Ferreras I., 2010, MNRAS, 405, 77  
 Schive H.-Y., Chiueh T., Broadhurst T., Huang K.-W., 2016, ApJ, 818, 89  
 Silk J., Mamon G. A., 2012, Res. Astron. Astrophys., 12, 917
- Smith R. J., Lucey J. R., Conroy C., 2015, MNRAS, 449, 3441  
 Sonnenfeld A. et al., 2017, Publ. Astron. Soc. Japan, preprint ([arXiv:1704.01585](https://arxiv.org/abs/1704.01585))  
 Springel V. et al., 2005, Nature, 435, 629  
 Taylor E. N. et al., 2011, MNRAS, 418, 1587

## SUPPORTING INFORMATION

Supplementary data are available at [MNRAS](https://mnras.oxfordjournals.org) online.

**Table 1.** Diagnostics of the selected models for each Space Warps candidate (see Section 6).

Please note: Oxford University Press is not responsible for the content or functionality of any supporting materials supplied by the authors. Any queries (other than missing material) should be directed to the corresponding author for the article.

## APPENDIX A: DEVELOPMENTS IN SPAGHETTILENS

### A1 Improved synthetic images

The mass maps produced by the current implementation of SpaghettiLens are based on images of point-like features. No information about extended images is used, except in so far as they help the user identify images of point-like features. The synthetic images offered to users are rudimentary, corresponding to conical light profiles (i.e. circular light profiles with brightness decreasing linearly with radius).

We have now developed a prototype to improve the generation of synthetic images, as illustrated in Fig. A1. Areas containing lensed images are selected (green frames in the figure). The selected areas should be as free as possible from other sources, including the lensing galaxy. Pixels within the selected areas are mapped to a grid on the source plane, using bending angles given by the mass model. The mapping from lens-plane pixels to source-plane grid cells is many-to-one, because of image multiplicity and magnification. The brightness of each source-plane pixel is set to the mean of all the lens-plane pixels mapped to it. Finally, the mapping is run back to the lens plane. The result is a synthetic image. In effect, one is reconstructing a source-plane brightness map by least squares.

The procedure is not yet implemented in SpaghettiLens but can be applied during post-processing. The new synthetic images could be used to improve the mass reconstruction, by weighing the ensemble of maps according to how good the synthetic images are.

### A2 Sub-sampling of the central region

The models of simulated lenses in Küng et al. (2015) showed a tendency to produce density profiles which were too shallow, resulting typically in overestimates of the Einstein radius. Allowing some extra mass tiles in central region, thus allowing the mass profile to rise more steeply near the centre, was suggested as a possible cure.

Fig. A2 shows an experiment with smaller mass tiles in the inner region. Replacing the very central mass tile with nine smaller tiles allows for steeper central profiles. Doing the same for the 25 innermost mass tiles allows for even steeper central profiles, eliminating the systematic shallow profiles. However, it does not provide a completely satisfactory solution, because (a) it increases the number of mass tiles by 40 per cent and significantly increases the computational time, and (b) the square boundary between areas with different tile sizes is rather undesirable. The main modelling

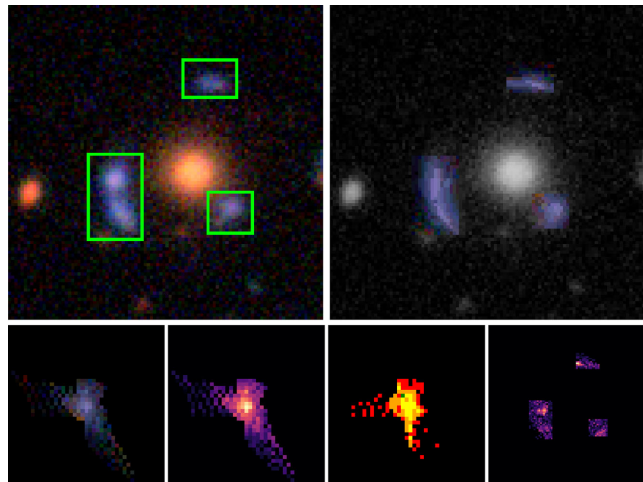


**Figure A1.** Synthetic lensed image with source-profile fitting in SW05 (J143454.4+522850). Top-left: original image, with areas containing lensed images enclosed within green frames. Top-right: synthetic image (coloured arcs) with lensing galaxy and unrelated objects in grey-scale. Bottom from left to right: reconstructed source in colour, intensity (grey-scale), and count of lens-plane pixels per source-plane pixel, and residual of original image to synthetic image.

work in this paper was, however, done before the experiment with smaller mass tiles was complete. Some of the models presented in this paper apply the intermediate option (corresponding to the middle panel in Fig. A2) while others use the old system. We note this paper mainly concerns the enclosed mass in the outer regions, so shallowness in the central region should not be an issue.

### A3 Parametrization of pixel models

In order to fit the set of pixelated models to a single parametrized model, a program was written that took a parametrized function and subtracted from it the mean and the principal components (PCs) of the data. This created the residual function. The number of PCs in the analysis was varied, to test how this affected the output. It was found that five PCs gave a reasonable approximation. A masking function was added, selecting only the data points that fell inside the image of the lens, and the PCs were clipped in order to keep the values inside the region of the ensemble. Any value higher than the clip was set to be the clip value. This was chosen to 2.5 because, assuming that the data follow a Gaussian error distribution, almost all the values for the variance should lie between 2 and 3 standard deviations from the mean. Minimizing the residuals function produces the set of parameters that fit the parametrized function to the original pixelated ensemble most closely. A least squares fit was used to perform this minimization. The parametrized model function was obtained from the gravitational potential of an isothermal ellipsoid mass distribution (Keeton 2001). This model is frequently used to describe gravitational lenses, giving good fits to the observations. The isothermal ellipsoid model outputs three useful parameters: the radius of the Einstein ring, the ellipticity of the model and the angle of the ellipticity from the vertical, giving the orientation of the galaxy. By applying this model to simulated lenses for which the values of these parameters were already known, it was possible to assess the accuracy of the methodology, before applying the model to the candidate lensing galaxies. Preliminary results on the recovery of Einstein radii are shown in Fig. A3.

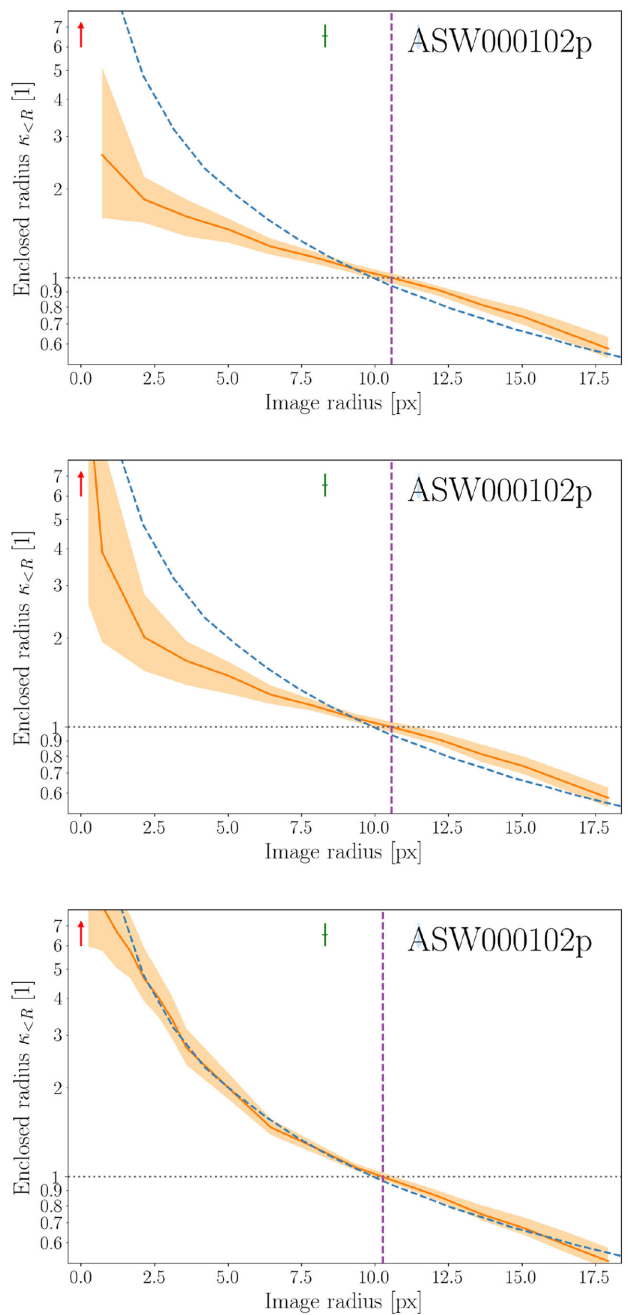


**Figure A2.** Model improvement resulting from the use of smaller mass tiles in the inner region of the mass model. Shown here are the average enclosed  $\kappa$  within a given projected radius, for three different reconstructions of a simulated lens (sim) from Space Warps. In each panel, the dashed blue curve is the correct answer. The orange band represents the statistical ensemble from SpaghettiLens, and the orange line shows the ensemble mean. Locations of images (maximum, saddle point, minimum) are marked with vertical arrows. The radial value at  $\kappa = 1$  is the effective Einstein radius,  $r_E$ . The upper panel is taken from Küng et al. (2015), see fig. 3 of that paper. The middle panel is the result when the innermost mass tile is replaced by nine smaller tiles. The lower panel results from replacing the innermost  $5 \times 5$  tiles with nine smaller tiles each.

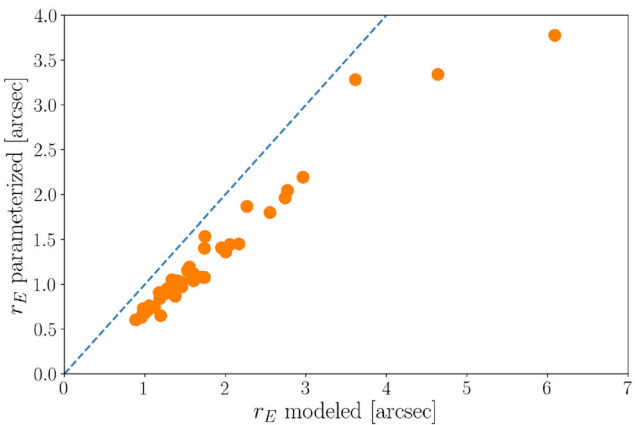


**Figure A3.** Comparison of Einstein radii  $r_E$  obtained from mass tiles to the results from a parametrized model to test the performance of the algorithm. The parametrized model was generated using principal component analysis on the ensemble of models. The blue dashed line represents a perfect recovery of  $r_E$ .

This paper has been typeset from a  $\text{\TeX}/\text{\LaTeX}$  file prepared by the author.